Applications in Energy and Combustion Science 17 (2024) 100238

Contents lists available at ScienceDirect

Applications in Energy and Combustion Science

journal homepage: www.sciencedirect.com/journal/applications-in-energy-and-combustion-science

Investigation of barium iron oxides for CO_2 capture and chemical looping oxygen uncoupling

Syed Saqline [a,b,c], Haiming Wang [c,d], Qianwenhao Fan [a,b], Felix Donat [e], Christoph Müller [e], Wen Liu [a,b,c,*]

[a] School of Chemistry, Chemical Engineering and Biotechnology, Nanyang Technological University, 637459, Singapore
[b] Cambridge Centre for Advanced Research and Education, 1 Create Way, #05-05, Singapore 138602, Singapore
[c] Nanyang Environmental and Water Research Institute, Nanyang Technological University, 1 Cleantech Loop, Singapore 637141, Singapore
[d] Department of Energy and Power Engineering, Tsinghua University, Beijing 100084, China
[e] Department of Mechanical and Process Engineering, ETH Zurich, Leonhardstrasse 21, 8092 Zürich, Switzerland

ARTICLE INFO

Keywords:
Barium ferrites
CO_2 sorbent
oxygen carrier
air separation
chemical looping

ABSTRACT

The performance of two underexploited ternary oxides – $Ba_3Fe_2O_6$ and $Ba_5Fe_2O_8$ are investigated for carbon dioxide capture and chemical looping oxygen uncoupling. The ternary compound $Ba_3Fe_2O_6$ was found to have a structure characterised by space group $Pa\bar{3}$. Experimental results have shown that both $Ba_3Fe_2O_6$ and $Ba_5Fe_2O_8$ are capable of cyclically capturing CO_2 at temperatures above 800 °C. $Ba_5Fe_2O_8$ demonstrated superior CO_2 capture performance compared to $Ba_3Fe_2O_6$, with consistent gravimetric CO_2 uptake capacities of 4.35 wt% and 13.39 wt% at 900 °C and 1000 °C, respectively, over 20 cycles. In comparison, $Ba_3Fe_2O_6$ demonstrated high initial CO_2 uptake capacities which deteriorated cyclically, with 20 cycle average capacities of 7.73 wt% and 11.99 wt% at 900 °C and 1000 °C, respectively. $Ba_3Fe_2O_6$ also exhibits excellent recyclability and satisfactory chemical looping oxygen uncoupling (CLOU) activity over temperature swing cycles between 550 °C and 950 °C. In contrast, the strong affinity with CO_2 makes $Ba_5Fe_2O_8$ unsuitable for application in chemical looping oxygen uncoupling or chemical looping air separation, especially in the presence of substantial partial pressures of CO_2.

1. Introduction

CO_2 constitutes the largest proportion of greenhouse gas emissions, with an estimated mean atmospheric lifetime of 300 years, while 25 % of CO_2 emissions last indefinitely [1]. Electricity and heat generation activities are responsible for approximately half of the total anthropogenic CO_2 emissions [2]. The combustion of fossil fuel emits many pollutants and poses a significant environmental risk due to activities associated with their procurement. Carbon dioxide (CO_2) emissions from industrial activities, particularly from the combustion of fossil fuels, have been identified as the primary cause of climate change [3]. In response, the development of effective technologies for capturing and storing CO_2 has emerged as an urgent solution to climate change. One such carbon capture technique is chemical looping (CL), which utilises solid intermediates to separate a desired reaction into two or more constituent reactions, preventing direct contact between reactants and enabling easier separation of the products of combustion [4]. This versatile approach can be applied to a variety of processes, including fossil fuel combustion, water splitting, air separation, and the synthesis of high-value products [5–8]. In general, chemical looping offers high energy conversion efficiency, reduces exergy losses, and provides safer operation by preventing the use of gaseous oxygen compared to conventional gas-phase redox chemical processes [6,9,10]. In most CL processes, a solid metal oxide, nitride, or hydride is used as an intermediate to transfer oxygen, nitrogen, or hydrogen, respectively, between individual reactors running different constituent reactions. These solid materials, commonly known as carriers, play crucial roles in chemical looping processes. While the interests in nitrogen and hydrogen carriers emerged recently, most of the carriers studied to date have been oxygen carriers (OCs) [8]. In the context of carbon capture and storage, the relevant CL processes include chemical looping combustion (CLC), chemical looping oxygen uncoupling (CLOU), chemical looping reforming, and chemical looping CO_2 capture (also known as sorbent looping or CO_2 looping).

* Corresponding author at: School of Chemistry, Chemical Engineering and Biotechnology, Nanyang Technological University, 637459, Singapore.
E-mail address: wenliu@ntu.edu.sg (W. Liu).

https://doi.org/10.1016/j.jaecs.2023.100238
Received 14 October 2023; Received in revised form 21 December 2023; Accepted 25 December 2023
Available online 26 December 2023

1.1. CO_2 looping

As depicted in Fig. 1(a), CO_2 looping is a cyclic process involving the reversible reaction between CO_2 and a metal oxide to form metal carbonates. The metal carbonate is subsequently decomposed to release CO_2 and regenerate the metal oxide, which can be used for further CO_2 capture. The reversible reactions by a generic bivalent metal carbonate are shown in reactions (1) and (2).

$$MeO\ (s) + CO_2\ (g) \rightarrow MeCO_3\ (s) \quad (1)$$

$$MeCO_3\ (s) \rightarrow MeO\ (s) + CO_2\ (g) \quad (2)$$

Natural minerals, such as limestone and dolomite have been used for the CO_2 looping processes, because of advantages such as their high reactivity, abundant availability, and low cost [11]. The use of synthetic oxides, including those Ca-based oxides and non-Ca-based oxides [11–16], for CO_2 looping can also enable the CO_2 looping process to efficiently capture CO_2 from a wide range of industrial processes with various operating temperatures and pressures (e.g. sorbent-enhanced reforming [17,18]). For post-combustion capture, CO_2 looping can be integrated with various power generation systems, including coal-fired power plants, natural gas power plants, biomass power plants, and waste-to-energy plants [19].

Various types of synthetic oxides have also been investigated for CO_2 looping, including monometallic oxides, mixed metal oxides, and doped oxides. The most common type of sorbents used in CO_2 looping are CaO and MgO [20,21]. CaO is widely utilised in CO_2 capture systems because of the low-cost and the availability of limestone and other Ca-rich minerals. Similarly, MgO can be produced from natural minerals such as magnesite, through relatively simple and energy-efficient production processes. Therefore, CO_2 looping process is often referred to as calcium looping (CaL). It has also been shown that the cost of carbon capture through CO_2 looping is on par with or even cheaper than amine scrubbing technology [22].

In addition to CaO/MgO-based sorbents, solid oxide sorbents based on other alkali and alkaline earth metals are also subjects of study for CO_2 capture at elevated temperatures [23–25]. The chemical properties of these materials can be tailored to optimise their CO_2 capture performance. Recently, ternary oxide sorbents have attracted substantial attention as potential contenders for CO_2 looping [26], e.g. Ca_2SiO_4, Li_4SiO_4, Li_2ZrO_3, Na_2ZrO_3 and $CaFeO_{2.5}$ [27–31]. These sorbents typically possess intricate crystal structures with diverse metal coordination environments, rendering them potentials for a broad spectrum of applications [29,32,33]. Additionally, ternary oxide sorbents have demonstrated superior stability over cycles of CO_2 capture and release compared to conventional oxide-based sorbents (e.g. CaO and MgO-based sorbents), owing to their robust resistance to sintering and their ability to retain their pore structure during the CO_2 looping process [12]. Furthermore, the inherent structural stability of the ternary oxide allows the A sites and B sites to be substitutionally doped without major structural changes, opening new avenues for synthetically optimising the sorbent performance. Therefore, the investigation of ternary oxide-based sorbents is important for developing effective CO_2 capture and storage processes with high CO_2 capture capacity, good cyclic stability, tuneable properties, and compatibility with a wide range of industrial applications. Further research is also needed to optimise their properties for improved CO_2 uptake and release kinetics, as well as long-term stability regenerability, before they can be commercially deployed for large-scale CO_2 capture.

1.2. Chemical looping oxygen uncoupling (CLOU)

Chemical looping oxygen uncoupling (CLOU) is a high temperature process exploiting principles similar to CLC, to produce oxygen-enriched process streams via the thermal decomposition of solid metal oxide carriers [5]. The uncoupling of oxygen is a two-step redox reaction:

$$Me_xO_{y-2}\ (s) + O_2\ (g) \rightarrow Me_xO_y\ (s) \quad (3)$$

$$Me_xO_y\ (s) \rightarrow Me_xO_{y-2}\ (s) + O_2\ (g) \quad (4)$$

Similar to CLC, CLOU can be achieved using two reactors, namely the oxidation reactor and the reduction reactor, in which reactions (3) and (4) take place, respectively. The CLOU scheme is illustrated in Fig. 1(b).

As shown in Fig. 1(b), fully oxidised metal oxides enter the reduction reactor and undergo reaction (4) in the presence of a carrying gas (usually steam or CO_2). The mixture of carrying gas and gaseous O_2 exiting the reduction reactor can be used as an oxidant for various applications (including oxy-fuel combustion). The reduced particles are recycled to the oxidation reactor where reaction (3) takes place in the presence of hot air. The oxygen-depleted air is then either used to preheat the incoming air or, in the case of pressurised operation, expanded in a gas turbine to generate power. In ideal conditions, the net heat released over the two reactions is zero. In this context, the oxygen carrier particles also serve as heat carriers to transport heat from the exothermic reaction (3) to the endothermic reaction (4).

Amongst the oxides of 3d transition metals, the most suitable candidates for CLOU are MnO_2/ Mn_2O_3, Mn_2O_3/Mn_3O_4, CoO/Co_3O_4, and CuO/Cu_2O. Besides monometallic metal oxides, ternary oxide materials can be also used as oxygen carriers for CLOU applications [34–36]. The tunability of the site occupancies and oxygen vacancies makes it easy to tailor the oxide structures for specific chemical looping applications. For example, when high oxygen partial pressures are desired, perovskites

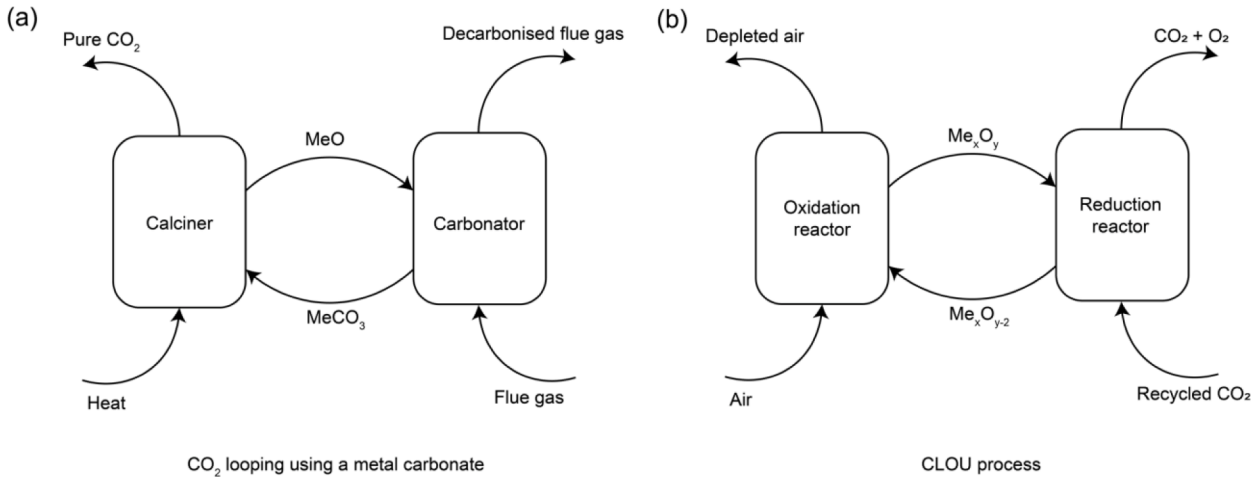

Fig. 1. Schematic illustration of **(a)** CO_2 looping using a metal carbonate **(b)** CLOU process.

such as $SrFeO_{3-\delta}$ can be used. The oxygen deficient $SrFeO_{3-\delta}$ was studied for hydrogen production and catalytic CH_4 combustion applications in TGA and fluidised beds [36]. The study showed reversible phase transitions between the perovskite and deep reduction products (viz. SrO and Fe). In addition, ternary oxides could potentially alleviating some of the problems and risks associated with conventional CLOU materials, such as loss of activity, deactivation due to thermal stress, attrition, agglomeration, and cost of OCs [37,38].

1.3. Ba-ferrite ternary oxides for chemical looping applications

Being the most earth-abundant and cheapest transition metal, iron-containing ternary oxides have received widespread research interest by the chemical looping community, with most research focusing on Ca, Sr, and Ba ferrite systems [39–42]. A unique feature of ternary oxides systems is the presence of Fe^{4+}, which is highly redox-active. In comparison, Fe generally takes +2 and +3 oxidation states in its native oxides, e.g., FeO, Fe_3O_4 and Fe_2O_3 [43]. A Mössbauer spectroscopy study examining the structure for the cubic perovskite $SrFeO_3$ confirmed the high valence of Fe. This compound was proven to be a metallic conductor due to the wide conduction bands and the strongly hybridised Fe-3d and O-2p orbitals [44]. Another alkaline earth metal ferrite, $CaFeO_3$ was also shown to exhibit similar conducting behaviour due to delocalisation of electrons [45,46].

Ternary oxides of Ba and Fe, e.g. $BaFeO_3$ has also been known to stabilise the Fe^{4+} [47]. They can be prepared by solid state reaction between magnetite and a barium precursor such as $BaCO_3$ and $Ba(NO_3)_2$ [47]. For chemical looping applications, $BaFe_2O_4$ has shown promising performance for chemical looping gasification of biochar [48]. Chen et al. [49] also used $BaFe_2O_4$ for chemical looping biomass gasification and found that an OC loading as low as 10 wt% (2 g fuel and 0.2 g OC) was able to produce higher hydrogen yield than other OC loadings tested (ranging from 0 to 50 wt%).

As shown in both the isopleth phase diagram (Fig. 2(a)) and the isothermal phase diagram (Fig. 2(b)) of the Ba-Fe-O system, moving from the Fe-rich side to the Ba-rich side on the left, the Ba-Fe-O system would form, in sequence, Fe_2O_3, $BaFe_{12}O_{19}$, $BaFe_2O_4$, $BaFeO_3$, $Ba_2Fe_2O_5$, $Ba_3Fe_2O_6$ and $Ba_5Fe_2O_8$ and BaO. While mixed Fe-rich barium ferrites such as $BaFe_2O_4$ and $BaFe_{12}O_{19}$ (barium hexaferrite, commonly used as a permanent magnet) have been studied for chemical looping applications [50], the phases at the Ba-rich end of the Ba-Fe-O system, e.g., $Ba_3Fe_2O_6$ and $Ba_5Fe_2O_8$, remain largely unexplored. Montorsi and Brisi [51] found that $Ba_3Fe_2O_6$ was stable in air above 800 °C (as seen in Fig. 2(a)). Below 800 °C, $Ba_3Fe_2O_6$ would decompose into Fe^{4+}-containing compounds, e.g., $BaFeO_3$. While the structure of $Ba_3Fe_2O_6$ was reported to be similar to that of $Sr_3Al_2O_6$ (space group $Pa\bar{3}$), $Ba_5Fe_2O_8$ has only been identified by calorimetry measurements with unresolved crystal structure [52,53]. Compared to Fe_2O_3, $BaFe_2O_4$ and $BaFeO_3$, the reducibility of $Ba_3Fe_2O_6$ and $Ba_5Fe_2O_8$ appears low, as suggested by Fig. 2(b). On the other hand, given the high Ba/Fe ratio, $Ba_3Fe_2O_6$ and $Ba_5Fe_2O_8$ are expected to have high basicity for CO_2 capture via carbonation to form $BaCO_3$.

In this paper, the two Ba-rich barium ferrite phases, viz. $Ba_3Fe_2O_6$ and $Ba_5Fe_2O_8$, are studied as CO_2 sorbents and oxygen carriers for CO_2 capture and chemical looping oxygen uncoupling (CLOU) [54], respectively. This work represents an exploratory effort to experimentally investigate the two Ba-rich ferrite phases for their potential applications in chemical looping processes.

2. Experimental

2.1. Materials synthesis

The two ternary oxides, i.e., $Ba_3Fe_2O_6$ and $Ba_5Fe_2O_8$, were prepared using the modified Pechini method. In a typical synthesis to prepare 1 g of barium ferrite sample, calculated amount of barium nitrate ($Ba(NO_3)_2$) and iron nitrate nonahydrate ($Fe(NO_3)_3{\cdot}9H_2O$) were dissolved in 150 ml Type II deionised (DI) water. The specific amounts of precursors used are shown in Table 1. The precursor solution was maintained at 50 °C on a heating plate with magnetic stirring at 300 rpm for 30 min. The chelating and crosslinking agents used were citric acid ($C_6H_8O_7$) and ethylene glycol ($C_2H_6O_2$), respectively. The specified amounts of these agents (see Table 1) were added to the solution. Then, the temperature of the solution was increased to 80 °C until a dark brown viscous gel formed. After gel formation, the stirring was stopped, and the gel was allowed to dry at 105 °C in a drying oven for at least 12 h. To remove the organic carbon, the dried gel was placed in a crucible and heated in a muffle furnace at 400 °C for 6 h. The organic components of this gel would devolatilise, decompose, and combust in the muffle furnace leaving behind a residue resembling a sponge like

Table 1
Amounts of precursors used for the synthesis of 1 g of barium ferrites.

Precursor	$Ba_3Fe_2O_6$ (amount in g)	$Ba_5Fe_2O_8$ (amount in g)
$Ba(NO_3)_2$	1.27	1.41
$Fe(NO_3)_3{\cdot}9H_2O$	1.30	0.87
Citric acid	3.88	3.63
Ethylene glycol	1.88	1.76

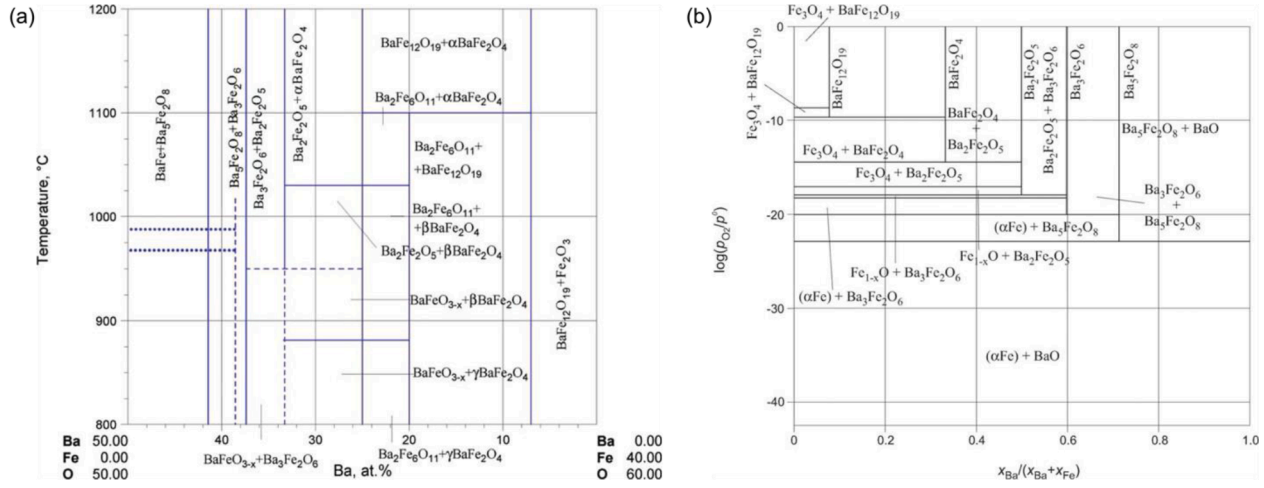

Fig. 2. **(a)** A quasi-binary section of BaO-Fe_2O_3 in air 800–1200 °C and **(b)** Phase diagram of the Ba-Fe-O system showing oxygen potential versus Ba/(Ba+Fe) ratio at 827 °C [53].

texture. This residue was ball milled in a Focucy planetary ball mill (F-P4000) for 2 h at ~400 rpm and sieved into size fraction of 100–200 μm. The sieved particles were subsequently calcined in air in a muffle furnace at 1000 °C for 15 h with a heating rate of 5 °C/min. The calcined samples were sieved again to the size fraction of 100–200 μm before testing. The oxide samples are named Ba_x, where x = 3 refers to $Ba_3Fe_2O_6$ and x = 5 refers to $Ba_5Fe_2O_8$.

2.2. Thermogravimetric analysis

The barium ferrites' ability to (a) reversibly take up CO_2 over CO_2 looping cycles and (b) release and take up gaseous oxygen over reduction-oxidation cycles was investigated by thermogravimetric analysis (TGA, Mettler Toledo TGA/DSC2 LF 1100). The TGA equipment consisted of an electrically heated high temperature furnace and a microbalance with an accuracy of 0.1 μg incorporated into the furnace to measure the mass of the sample. Calibrated rotameters were utilised to regulate the flow rates of both the purge gas and protective gas.

2.3. CO_2 uptake

In a typical CO_2 looping experiment, approximately 50 mg powdered sample was loaded into a 150 μL alumina pan, which was inserted into the reaction chamber of the TGA. During each experiment, the sample was firstly heated from ambient temperature to the reaction temperature, which ranged between 800 and 1000 °C, while purged by pure N_2 gas flowing at a rate of 50 ml/min. At the reaction temperature, the sample was alternatingly exposed to CO_2 and N_2 gases, each flowing at 50 ml/min for 30 min, for 20 cycles. Therefore, each CO_2 uptake-regeneration cycle was 60 min. Based on the recorded weight changes, the CO_2 capture efficiency of the sorbents is estimated according to:

$$\eta_{CO2,up} = \frac{\text{observed mass change per cycle, averaged over 20 cycles}}{\text{stoichiometric } CO_2 \text{ uptake capacity}} \times 100\% \quad (5)$$

where the stoichiometric CO_2 uptake capacity, in mass basis (i.e. mass of CO_2 taken up/mass of the fully calcined sample), is calculated based on the following reactions:

$$Ba_3Fe_2O_6 + 2CO_2 \leftrightharpoons 2BaCO_3 + BaFe_2O_4 \quad (6)$$

$$Ba_5Fe_2O_8 + 4CO_2 \leftrightharpoons 4BaCO_3 + BaFe_2O_4 \quad (7)$$

Separately, the experimentally measured CO_2 uptake capacity, also referred to as the gravimetric CO_2 uptake capacity in $mg_{CO2}/g_{sorbent}$, is defined by the ratio of weight gain by the sample during carbonation relative to its minimum weight measured during calcination, within a CO_2 capture-regeneration cycle.

2.4. Chemical looping oxygen uncoupling

In a typical CLOU experiment, approximately 50 mg of powdered sample was put in a 150 μL alumina pan, which was subsequently inserted into the reaction chamber of the TGA, where the sample was exposed to alternating oxidising (50 ml/min of air at 550 °C) and reducing (50 ml/min of N_2 at 950 °C) environments. Once the sample temperature reached the set points of 550 °C and 950 °C, the sample was immediately heated up or cooled down at a rate of 10 °C /min, respectively, without any isothermal dwelling. Based on the measured weight changes, the O_2 release efficiency of the sorbents is estimated according to:

$$\eta_{O2,rel} = \frac{\text{observed mass change per cycle, averaged over 20 cycles}}{\text{stoichiometric } O_2 \text{ release capacity}} \times 100\% \quad (8)$$

where, the stoichiometric O_2 release capacity is calculated based on the following reactions:

$$2BaFeO_3 + BaO \leftrightharpoons Ba_3Fe_2O_6 + 0.5O_2 \quad (9)$$

$$2BaFeO_3 + 3BaO \leftrightharpoons Ba_5Fe_2O_8 + 0.5O_2 \quad (10)$$

2.5. Material characterisation

2.5.1. X-ray diffraction

Powdered XRD spectra at room temperature and pressure were collected using a Bruker D8 Advance diffractometer with filtered Cu Kα radiation (λ = 1.5418 Å) at 40 kV and 40 mA under ambient conditions. The XRD patterns were collected in a 2θ range from 10 to 90° with a step size of 0.02° and a collection time of 1 s/step.

The *in situ* XRD measurements were carried out with a PANalytical Empyrean X-ray powder equipped with a X'Celerator Scientific ultra-fast line detector and Bragg-Brentano HD incident beam optics using Cu Kα radiation (45 kV and 40 mA). The instrument is fit with an Anton Paar XRK 900 reactor chamber with a Macor sample holder in reflection geometry and gas flow through the sample with uniform temperature control. A 2θ range of 20°–80° with a scanning speed of 0.022° s^{-1} and a step size of 0.016° was employed. Phase identification was performed with the help of Match! V3.0 software.

In situ XRD measurements were performed to investigate the phase transitions of the barium ferrites at high temperature chemical looping cycles. To confirm the successful formation of the barium ferrite phases, the fresh samples were measured by XRD while being heated in air from 500 to 900 °C. Similarly, to explore the phase transitions of $Ba_3Fe_2O_6$ during CO_2 uptake, XRD measurements were conducted when the sample was firstly heated in air at 550 °C, then exposed to a mixture of 20 % CO_2 in N_2 for 20 min. The CO_2 mole fraction of 20 % was chosen because it is the upper limit that the *in situ* XRD reaction chamber could tolerate. The temperature was subsequently raised to 900 °C under the same gas mixture and sustained in 900 °C for a further 60 min, followed by a further XRD measurement. Finally, the inlet gas was switched to N_2 for an additional 60 min at 900 °C to simulate the sorbent regeneration, before the last XRD pattern was measured.

2.5.2. Scanning electron microscopy

The microstructure and morphological features of the ternary oxide samples were analysed using field emission scanning electron microscopy (FESEM). The measurements were carried out on a JEOL JSM-7200F electron microscope. The imaging was done at an accelerating voltage of 5 kV under low vacuum and room temperature conditions. Prior to imaging, the samples were mounted onto cylindrical aluminium sample holders using sticky carbon tape. The samples were then sputter coated with a thin layer of platinum using a sputter coater to increase the conductivity and enhance the contrast of the samples. A JEOL JEC-30000FC sputter coater was used for this purpose. The sputter coating was carried out at a current of 20 mA for 60 seconds. The magnification of the SEM images ranged from x100 to x20,000 depending on the morphological features of interest.

The SEM-EDX (energy-dispersive X-ray) analysis was performed with the above-mentioned FESEM unit equipped with an Oxford Instruments X-Max N EDX detector. The SEM was operated at an acceleration voltage of 20 kV. The SEM-EDX data was acquired using the Aztec software package. The software was used to control the SEM and EDX detector, and to acquire SEM images and EDX spectra from the sample. EDX spectra were collected from multiple areas of interest, and elemental maps were generated to visualise the spatial distribution of the elements.

3. Results and discussions

3.1. Structural characterisation

The energy-dispersive X-ray spectroscopy (EDX) analysis of the Ba_3 and Ba_5 samples, as shown in Fig. 3, confirms the elemental composition of the samples, i.e. the relative contents of Ba, Fe, and O are in accordance with the target stoichiometries (i.e. 66.5 wt% and 74.1 wt% barium for Ba_3 and Ba_5, respectively). The Pt signals in the EDX spectra arises from the Pt sputter coating during sample preparation for SEM. Therefore, the synthesis was deemed successful in producing samples with the correct stoichiometry, of $Ba_3Fe_2O_6$ and $Ba_5Fe_2O_8$ at high temperatures.

We examine the phase composition of the synthesised barium ferrite samples by means of *in situ* XRD. As seen in Fig. 4(a), the XRD spectra of Ba_3 at different temperatures show that the sample exhibited two distinct phases, namely $BaFeO_3$ and $BaCO_3$, in the temperature range of 500-800 °C. Above 800 °C, a unique set of peaks attributed to $Ba_3Fe_2O_6$ were observed, indicating that $Ba_3Fe_2O_6$ is only stable above temperatures of 800 °C. The unit cell of the $Ba_3Fe_2O_6$ lattice is shown in Fig. 4(b); it is isostructural to $Sr_3Al_2O_6$, belonging to the $Pa\bar{3}$ space group [53].

For Ba_5, two distinct phases of $BaFeO_3$ and $BaCO_3$ are also seen the range of 500-800 °C, as shown in Fig. 4(c). Similarly, phase change was observed above 800 °C, when the mixture of $BaFeO_3$ and $BaCO_3$ was replaced with a set of unindexed peaks. Given the unsolved crystal structure of $Ba_5Fe_2O_8$ [52], it is not entirely certain whether $Ba_5Fe_2O_8$ has truly formed, despite the calorimetric observation by Montorsi and Brisi [51]. Nevertheless, the phase transition at 800 °C is in line with the isopleth Ba-Fe-O phase diagram shown in Fig. 2(a). Based on the *in situ* XRD results, the phase transitions observed can be summarised by Eqs. (11) & (12), and denoted by the black arrows shown in the magnified triangular phase diagram of the Ba-Fe-O system, in Fig. 4(e). Notably, the phase transitions involve transformation of Fe^{4+} containing phases (e.g. $SrFeO_3$) to Fe^{3+} containing phases (e.g. $Ba_3Fe_2O_6$ and $Ba_5Fe_2O_8$) as the temperature increases beyond 800 °C.

$$2BaFeO_3 + BaCO_3 \leftrightharpoons Ba_3Fe_2O_6 + CO_2 + 0.5O_2 \quad (11)$$

$$2BaFeO_3 + 3BaCO_3 \leftrightharpoons Ba_5Fe_2O_8 + 3CO_2 + 0.5O_2 \quad (12)$$

3.2. CO_2 capture experiments

3.2.1. TGA performance of CO_2 uptake at 1000 °C

Fig. 5(a) shows the cyclic performance of both Ba_3 and Ba_5 at 1000 °C over 20 cycles in alternating atmosphere of CO_2 (simulating carbonation) and N_2 (simulating calcination). $Ba_3Fe_2O_6$ exhibited a notable decay in CO_2 uptake capacity, which may be attributed to the apparent deterioration in carbonation kinetics. Specifically, the carbonation of $Ba_3Fe_2O_6$ was rapid during the first cycle, reaching a uptake of 142 mg CO_2/g sorbent within 600 s. However, by the 20th cycle, a relative weight gain of only 96.1 mg CO_2/g sorbent was reached within 600 s. On the other hand, the apparent kinetics of regeneration (i.e., decomposition of $BaCO_3$) of Ba_3 appears consistent and fast over the 20 cycles. The average gravimetric CO_2 uptake capacity of $Ba_3Fe_2O_6$ over the 20 CO_2 capture cycles (as shown in Fig. 5(a) & 5(b)) was 127.88 mg CO_2/g sorbent. It should be noted that, given the limitation of the TGA instrument, which only allowed us to perform multiples of 5-cycle programmes with small pauses in-between, the samples were subjected to a longer calcination period every five cycle, resulting in a lower calcined mass and subsequently higher apparent gravimetric CO_2 uptake capacity for every 5 cycles.

$Ba_5Fe_2O_8$ exhibits slower carbonation during the initial 10 cycles (see Fig. 5(a)). Interestingly, the carbonation kinetics gradually accelerated over cycles, resulting in increased cyclic CO_2 uptake, as shown in Fig. 5(b). The cycle-averaged gravimetric uptake capacity of Ba_5 is

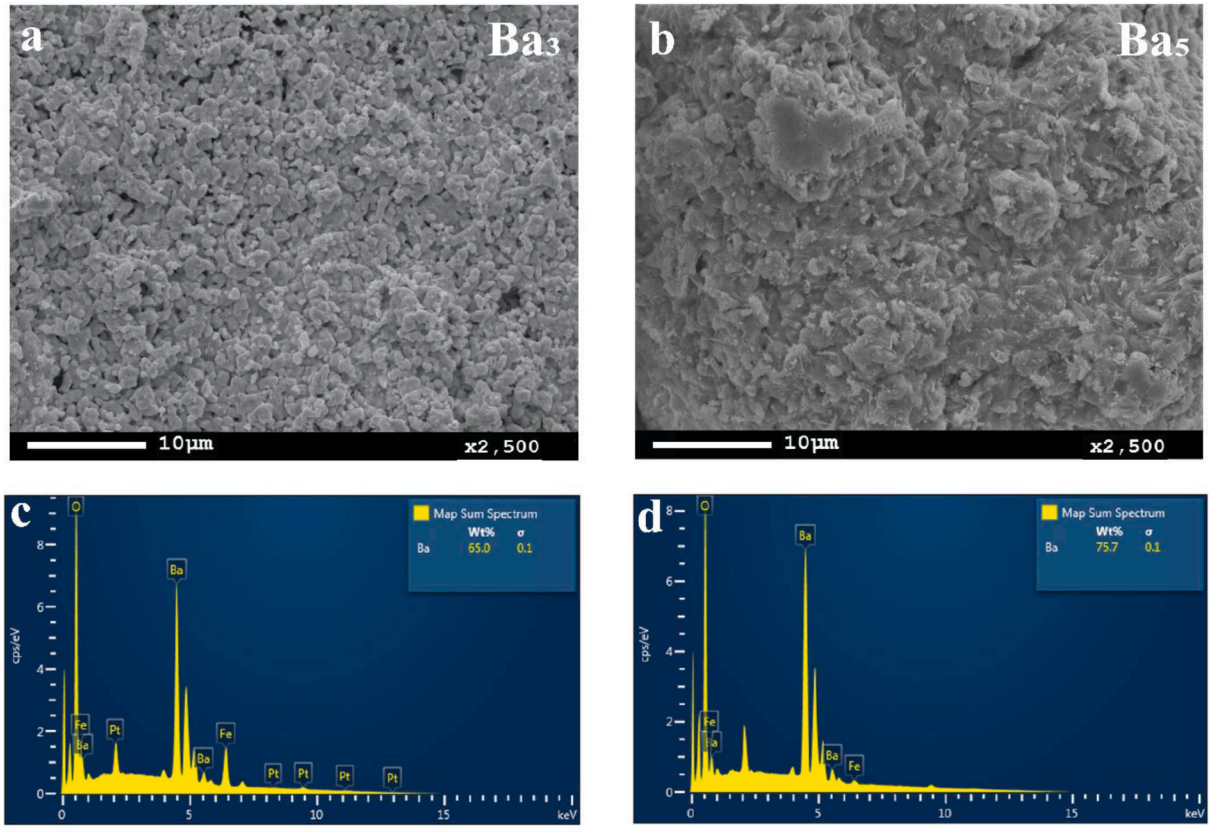

Fig. 3. SEM images of (a-b) fresh samples of Ba_3 and Ba_5, respectively and (c, d) EDX map spectrum of Ba_3 and Ba_5, respectively.

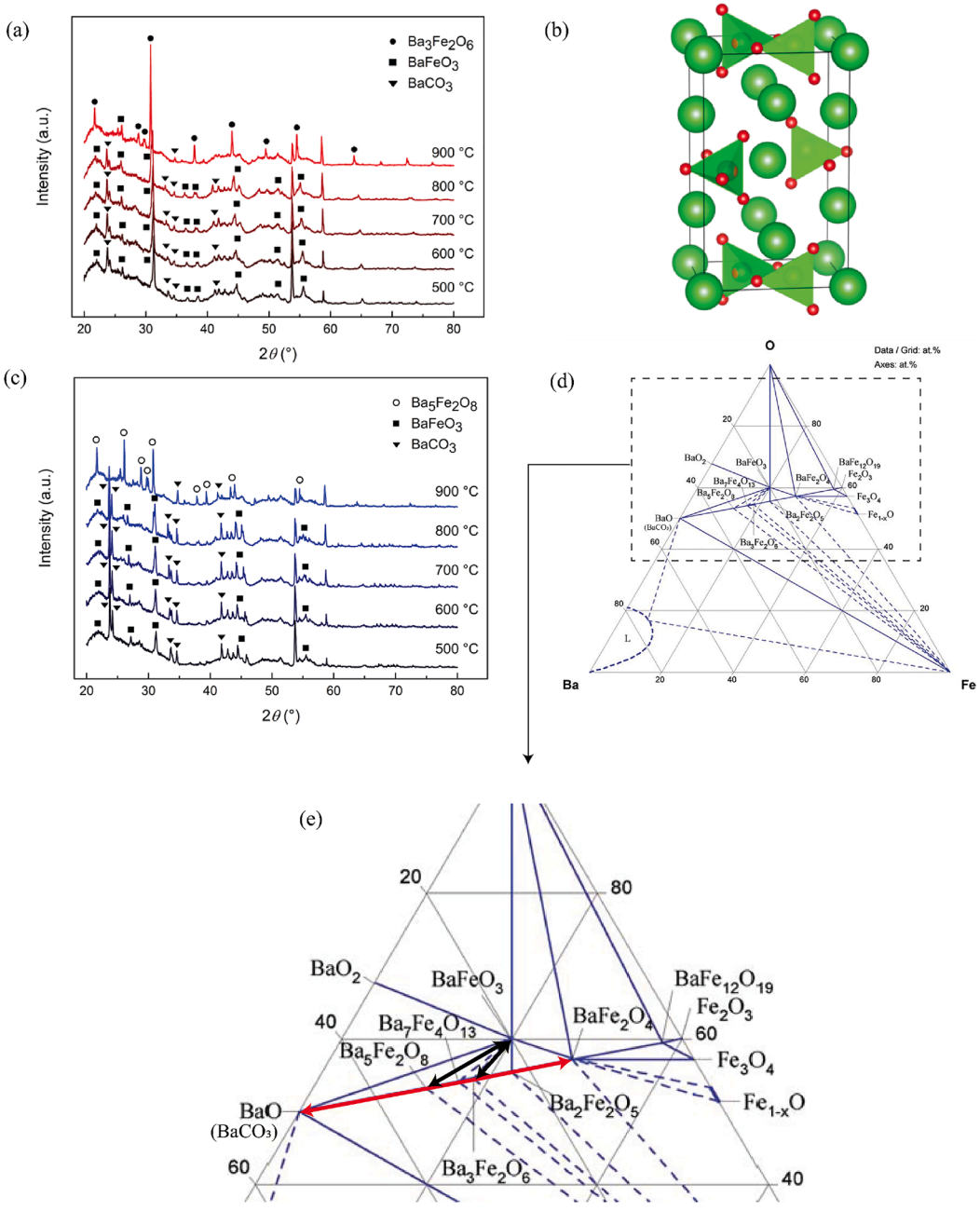

Fig. 4. (a) *In situ* XRD diffraction spectra of Ba_3 in air from 500 to 900 °C (b) Unit cell of $Ba_3Fe_2O_6$ (c) *in situ* XRD diffraction spectra of Ba_5 in air from 500 to 900 °C (d) Isothermal section of the Ba-Fe-O system for temperatures between 700 and 1000 °C. (e) a zoomed-in view of the triangular phase diagram [53].

147.5 mg CO_2/g sorbent. The decomposition kinetics of Ba_5 remained consistently fast, suggesting that the irreversible changes in the ternary oxides that are responsible for the changes in carbonation kinetics do not affect the decomposition kinetics. In addition, the fact that the apparent change in carbonation kinetics could be captured over CO_2 looping cycles suggests that the TGA measurements were not dominated by mass transfer effects.

Based on the measured maximum gravimetric CO_2 uptake capacities of 265 mg CO_2/g sorbent wt% and 271 mg CO_2/g sorbent for Ba_3 and Ba_5, respectively, the following reaction stoichiometries are proposed:

$$Ba_3Fe_2O_6 + 2CO_2 \leftrightharpoons 2BaCO_3 + BaFe_2O_4 \quad (13)$$

$$Ba_5Fe_2O_8 + 4CO_2 \leftrightharpoons 4BaCO_3 + BaFe_2O_4 \quad (14)$$

Reactions (13) and (14) corresponds to gravimetric CO_2 uptake capacities of 284 mg CO_2/g sorbent and 379.80 mg CO_2/g sorbent, respectively. Using the cycle-averaged CO_2 uptake capacities of 239.80 mg CO_2/g sorbent and 267.80 mg CO_2/g sorbent, the CO_2 capture efficiencies, $\eta_{CO2,up}$ of Ba_3 and Ba_5 are calculated to be 84.43 % and 70.51 %, respectively.

3.2.2. *Effect of operating temperature on CO_2 looping performance*

To examine the impact of operating temperature on the CO_2 capture performance of $Ba_3Fe_2O_6$ and $Ba_5Fe_2O_8$, 20 isothermal CO_2 swings were performed at 800 and 900, in addition to 1000 °C. All experimental results are shown in Fig. 6.

For Ba_3 (Fig. 6(a)), the weight change curve measured at 900 °C is similar to that of 1000 °C. At 900 °C, the rate of carbonation appears more rapid, but also undergoes obvious cyclic deactivation, probably owing to sintering. Overall, the CO_2 capture capacities at 900 °C are in

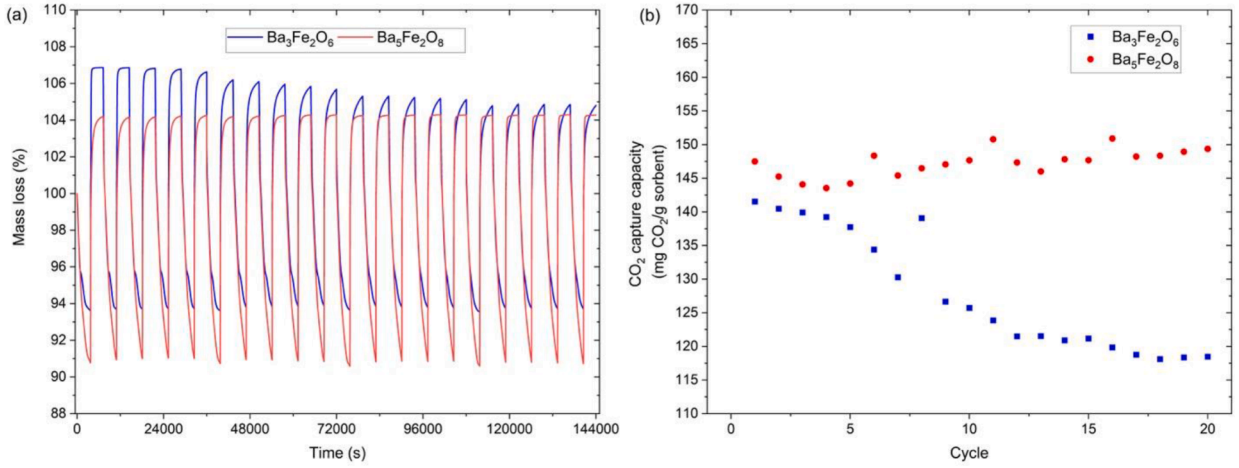

Fig. 5. **(a)** Relative mass change and **(b)** gravimetric CO_2 capture capacity of the two samples over 20 carbonation-calcination cycles in TGA at 1000 °C in alternating CO_2 and N_2 environment.

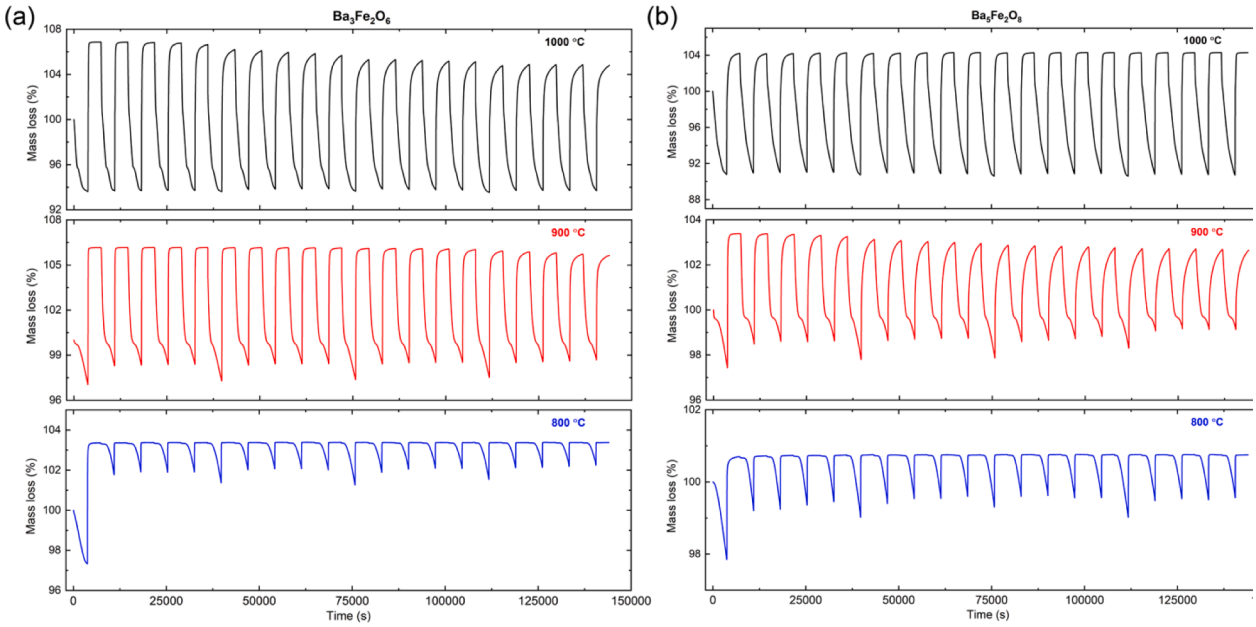

Fig. 6. Relative mass change over carbonation-calcination cycles, facilitated by alternating CO_2 and N_2 environment isothermally at 800, 900 and 1000 °C in a TGA for **(a)** $Ba_3Fe_2O_6$ and **(b)** $Ba_5Fe_2O_8$.

the range of 70–80 mg CO_2/g sorbent ($\eta_{CO2,up}$ = 48.19 - 55.07 %). At 800 °C, Ba_3 showed much lower CO_2 uptake capacity, in the range of 12–16 mg CO_2/g sorbent. In fact, Ba_3 appears to stay in a largely carbonated state at 800 °C with rather sluggish calcination. This observation is in line with the *in situ* XRD results shown in Fig. 4(a), which suggests that Ba_3 consists of a mixture of $BaCO_3$ and $BaFeO_3$ at 800 °C. The residual activity registered at 800 °C is attributed to the reversible carbonation of a small fraction of BaO or $BaFeO_3$. In general, Fig. Fig. 6(a) shows that calcination is kinetically hindered at lower temperatures, i.e., CO_2 looping employing Ba_3 should be preferably carried out at >800 °C.

For $Ba_5Fe_2O_8$ (Fig. 6(b)), contrasting the trend observed at 1000 °C, the CO_2 looping performance at 900 °C showed cyclic deactivation, with CO_2 uptake capacity falling from 49.76 mg CO_2/g sorbent ($\eta_{CO2,up}$ = 25.79 %) in the first cycle the 1st cycle from to 35.61 mg CO_2/g sorbent ($\eta_{CO2,up}$ = 18.59 %) in the 20th cycle. This decay appears to be associated with the increasingly sluggish carbonation kinetics, probably as a result of sintering and the significant resistance to mass transfer through the product layer. Similar to Ba_3, the performance of Ba_5 at 800 °C is limited owing to high stability of the $BaCO_3$, which were difficult to decompose. The highest weight changes (i.e., gravimetric CO_2 uptake capacities) observed at 800 °C and 900 °C were 1.96 % and 7.87 %, respectively. Interestingly, the sintering-induced deactivation that is apparent at 900 °C seems less obvious in experiments at 1000 °C, although the samples are expected to sinter more at higher temperature. This disparity may be attributed to the presence of other rate-enhancing factors at higher temperatures such as faster ionic diffusion through the carbonate product layer, which could alleviate the rate-inhibition effects induced by sintering. Therefore, both Ba-rich barium ferrite phases are suitable reversible CO_2 sorbents for high temperature CO_2 capture cycles (i.e., >900 °C).

3.2.3. *Mechanism of carbonation and calcination*

Between the two ternary oxides investigated, the crystal structure of $Ba_3Fe_2O_6$ has been resolved. Regardless, *in situ* XRD analysis was performed on both the ternary oxides to further investigate the phase

transitions occurring during high-temperature CO_2 looping cycles. The resulting diffraction patterns of Ba_3 and Ba_5 ternary oxides are shown in Fig. 7(a) and (b).

From Fig. 7(a), it can be seen that after 20 min carbonation in 20 % CO_2 at 550 °C, Ba_3 primarily consisted of $BaFeO_3$, in agreement with the TGA results. Upon increasing the temperature to 900 °C, while keeping the gas environment as 20 % CO_2, the $BaCO_3$ phase transitioned from an orthorhombic structure (Pmcn) to a trigonal one (Fm-3m), resulting in a change in the diffraction pattern. This phase transition of $BaCO_3$ typically occurs at 811 °C, according to Antao and Hassan [55]. The reference XRD patterns along with the crystal structures of the two encountered $BaCO_3$ phases are shown in Fig. 7(c) and (d). $BaFe_2O_4$ is also detected upon high temperature carbonation, in agreement with Eq. (13). After carbonation at 900 °C for 60 min, the atmosphere was switched to N_2 for 60 min at 900 °C to facilitate calcination. During calcination, $Ba_3Fe_2O_6$ was regenerated. The changes observed via the *in situ* XRD measurements validate that the cyclic carbonation and calcination of Ba_3 indeed follows Eq. (13).

Unlike Ba_3, the low temperature carbonation of Ba_5 C in 20 % CO_2 at 550 ° for 20 min resulted in $BaCO_3$ and $BaFe_2O_4$ (Fig. 7 (b)), corroborating the proposed carbonation mechanism in Eq. (14). Similar to the case of Ba_3, $BaCO_3$ formed from Ba_5 underwent a phase transition from an orthorhombic structure (Pmcn) to a trigonal one (Fm-3m). Calcination of the Ba_5 sample at 900 °C in N_2 for 60 min resulted in the extensive formation of $Ba_3Fe_2O_6$. Despite the similarity in forming $Ba_3Fe_2O_6$ upon calcination, the two barium ferrite phases behaved differently over CO_2 looping cycles, as shown in Figs. 5 and 6. The nature, the origin and the consequence of this difference ought to be further investigated in future studies. In addition, the fate of the excess Ba in the calcined Ba_5 is also a subject for future investigations.

3.2.4. Morphological changes over CO_2 looping cycles

In chemical looping systems, the activity and performance of the CO_2 sorbents and oxygen carriers are almost always affected by the morphologies (including porosity and surface area) of the looping materials. Accordingly, the morphological changes of the barium ferrite samples over CO_2 capture cycles were examined by SEM and BET analysis.

Fig. 8 shows the SEM images of Ba_3 and Ba_5 before and after 20 redox cycles of CO_2 capture. Fig. 8(a) and (b) show that the freshly prepared samples are porous, consisting of mesoporous aggregates of grains of size 2 –4 μm and 3–5 μm for Ba_3 and Ba_5, respectively. These porous structures give rise to moderately high BET surface areas, as shown in Table 2, which in turn result in faster carbonation kinetics during the first few CO_2 looping cycles. After cycling, the porous structure was replaced by a dense one, while the specific surface area of Ba_3 dropped drastically from 8.8 m^2/g to 0.87 m^2/g; both are obvious signs of sintering, accommodated by the significantly slowed carbonation kinetics, as shown in Fig. 5(a). Interestingly, the calcination kinetics were not affected by the reduction in BET surface area. This observation resembles the disconnection between severe sintering and stable CO_2 uptake performance reported by an earlier studying using $Ba_4Sr_2O_9$ as the CO_2 sorbent [12].

For Ba_5, the fresh sample also displayed a moderately high surface area of 12 m^2/g. After 20 cycles of CO_2 capture at 900 °C, the surface of Ba_5 appears to have lost most of its porosity, showing signs of severe sintering (Fig. 8(d)). Similarly, the specific surface area of the cycled Ba_5 dropped to 1.93 m^2/g after CO_2 cycling (Table 2). Therefore, sintering is responsible for the decaying performance of Ba_5 during CO_2 looping cycles at 900 °C, as shown in Fig. 6. Nevertheless, the severe sintering does not seem to affect the CO_2 uptake by Ba_5 at 1000 °C.

3.3. Chemical looping oxygen uncoupling

3.3.1. Oxygen release and uptake performance in TGA

The chemical looping oxygen uncoupling (CLOU) performance of the barium ferrite samples was also investigated by TGA. Each CLOU cycle

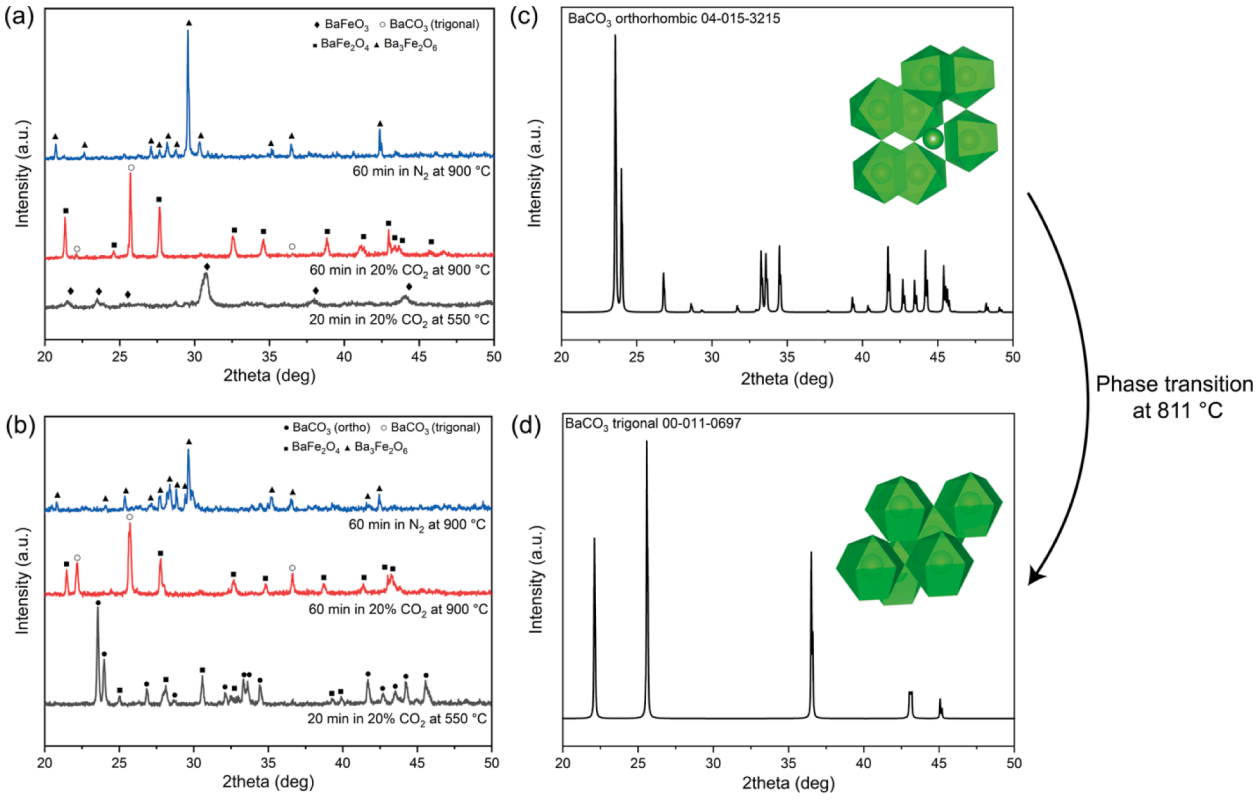

Fig. 7. *In situ* XRD pattern of **(a)** $Ba_3Fe_2O_6$ and **(b)** $Ba_5Fe_2O_8$, after being exposed to 20 min in 20 % CO_2 at 550 °C, followed by 60 min in 20 % CO_2 at 900 °C, and subsequently 60 min in N_2 at 900 °C. Reference XRD spectra and crystal lattice of $BaCO_3$ in (c) orthorhombic form and (d) trigonal form.

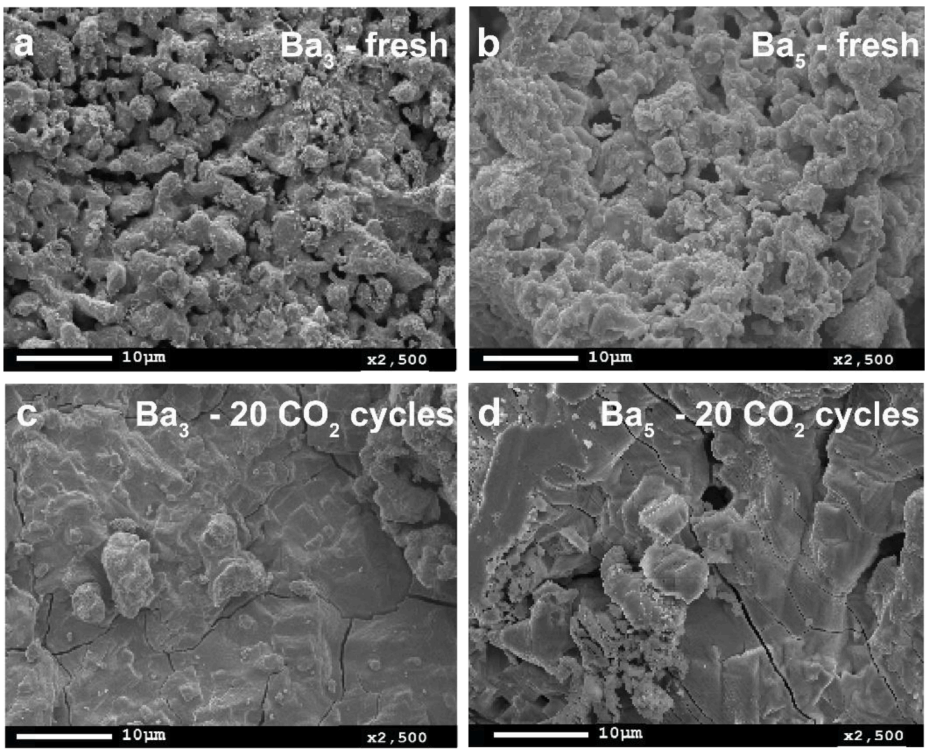

Fig. 8. SEM images of (a) and (b) - fresh samples, (c) and (d) after 20 cycles of CO_2 capture at 900 °C.

Table 2
BET surface area and pore size of the fresh and spent samples post CO_2 looping in TGA.

Sample	Surface area (m^2/g)	Pore size (nm)
Fresh $Ba_3Fe_2O_6$	8.8	8.30
Fresh $Ba_5Fe_2O_8$	12	10.96
Spent CO_2 looping $Ba_3Fe_2O_6$	0.87	20.85
Spent CO_2 looping $Ba_5Fe_2O_8$	1.93	24.50

consists of (1) air oxidation while heating up from 550 to 950 °C at 10 °C/min followed by (2) N_2 decomposition while cooling down from 950 to 550 °C at 10 °C/min, as shown in Fig. 9. The kinetics of both reduction and oxidation of Ba_3 were fast and consistent over 10 cycles. The observed mean mass change of Ba_3 is 1.25 wt% over the 10 redox cycles. Based on stoichiometry, the following oxygen release reactions are proposed:

$$2BaFeO_3 + BaO \leftrightharpoons Ba_3Fe_2O_6 + 0.5O_2 \quad (15)$$

$$2BaFeO_3 + 3BaO \leftrightharpoons Ba_5Fe_2O_8 + 0.5O_2 \quad (16)$$

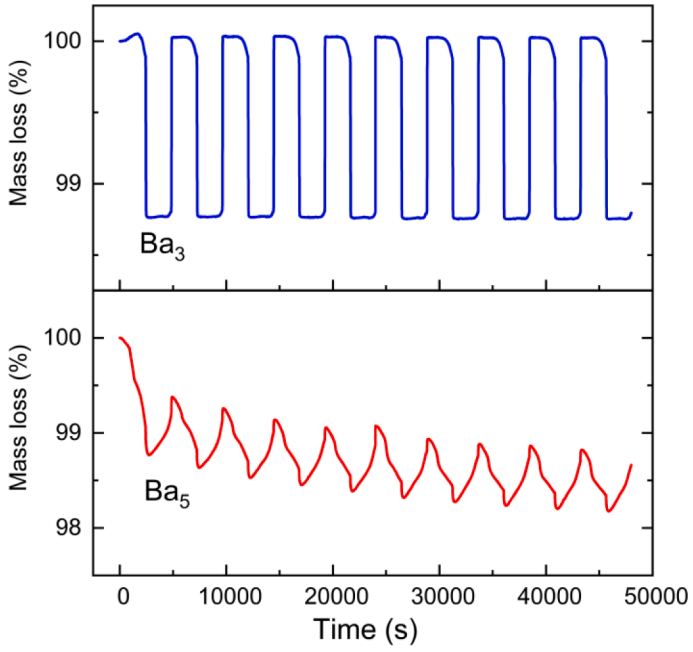

Fig. 9. Cyclic oxygen uncoupling in a coupled temperature and pressure swing between 550 °C in air and 950 °C in N_2.

Based on the stoichiometries shown in Eqs. (11) and (12), the theoretical gravimetric capacities of Ba_3 and Ba_5 are 2.52 wt% and 1.70 wt%, respectively. Based on these theoretical capacities, the cycle-averaged oxygen release efficiency, $\eta_{O2,rel}$ of Ba_3 was 49.60 %. The gravimetric O_2 uptake and release by Ba_5 were much lower than those by Ba_3, partly owing to the less favorable reaction stoichiometry, as shown in reactions (15) and (16), which is largely governed by the Fe content in the ternary oxide. The observed mean mass change of Ba_5 is 0.67 wt% over the 10 redox cycles. Based on Eq. (16), the cycle-averaged oxygen release efficiency $\eta_{O2,rel}$ of Ba_5 is 39.41 %. This low $\eta_{O2,rel}$, as well as the apparently sluggish kinetics of both the O_2 uptake and release, as shown in Fig. 9, may be attributed to the ability of Ba_5 to easily take up CO_2 to form $BaCO_3$ (instead of ternary oxides such as $BaFeO_3$), which hinders the CLOU activity of Ba_5. Therefore, between the two Ba-rich barium ferrite phases, $Ba_3Fe_2O_6$ shows more promising CLOU activity at high temperature, making it a potential candidate for applications such as CLOU and chemical looping air separation (CLAS).

3.3.2. *Morphological changes over CLOU cycles*

Fig. 10(a) & (b) shows the SEM images of the spent Ba_3 and Ba_5, respectively, over 20 cycles of CLOU between 550 and 950 °C. Interestingly, spent Ba_3 after CLOU experiments showed a surface morphology resembling that of the fresh sample (Fig. 10(a)). The preservation of the pore structure is corroborated by the high BET surface area of the spent Ba_3 of 15.02 m^2/g compared to that of the fresh Ba_3 (8.80 m^2/g, as shown in Table 3). However, for Ba_5, the spent sample exhibits signs of sintering, as characterised by large grains with smooth surfaces (annotated by the solid arrow shown in Fig. 10(b)), which are surrounded by small grains (annotated by the dashed arrow in Fig. 10 (b)). These large, non-porous grains could be assigned to the low-melting $BaCO_3$ phases, while the smaller grains could be $BaFeO_3$ or $Ba_2Fe_2O_5$. Overall, a slight decrease in surface area is observed for Ba_5 (12.11 to 10.96 m^2/g), shown in Table 3. The apparent presence of $BaCO_3$, which are also suggested by the TGA results, indicate that Ba_5 is not a suitable oxygen carrier for CLOU-related applications.

4. Conclusions

CO_2 looping and CLOU processes rely on the availability of high-performance CO_2 sorbents and oxygen carriers, respectively. In this paper, two barium ferrite samples, namely Ba_3 and Ba_5 with nominal compositions of $Ba_3Fe_2O_6$ and $Ba_5Fe_2O_8$ were investigated for their potential applications in CO_2 looping and CLOU, both of which are process schemes to capture CO_2 using the principle of chemical looping. The two compounds were unexplored for chemical looping applications in the literature. Specifically, the crystal structure of $Ba_5Fe_2O_8$ remains unresolved.

Table 3
BET surface area and pore size of the fresh and spent samples post oxygen release in TGA.

Sample	Surface area (m^2/g)	Pore size (nm)
Fresh $Ba_3Fe_2O_6$	8.80	8.30
Fresh $Ba_5Fe_2O_8$	12.11	10.96
Spent O_2 release $Ba_3Fe_2O_6$	15.02	5.31
Spent O_2 release $Ba_5Fe_2O_8$	10.96	13.79

Based on the results of TGA experiments, both Ba_3 and Ba_5 have demonstrated satisfactory performance to cyclically capture CO_2 at 900 °C and 1000 °C, forming mixtures of $BaCO_3$ and $BaFe_2O_4$ after carbonation. Between the two barium ferrites, Ba_5 shows superior and more stable CO_2 capture performance with average gravimetric CO_2 uptake capacities of 4.37 wt% and 13.39 wt% at 900 °C and 1000 °C, respectively. In comparison, Ba_3 shows gravimetric CO_2 uptake capacities of 7.79 wt% and 11.99 wt% at 900 °C and 1000 °C, respectively. The decay in the cyclic CO_2 capture capacity of Ba_3 was attributed to sintering. Both barium ferrites are only effective in capturing CO_2 above 800 °C. Below 800 °C, the Ba-rich barium ferrites are stable in the form of $BaCO_3$.

Because of the outstanding ability of Ba_5 to take up CO_2, it does not appear to be a suitable oxygen carrier for CLOU-related applications, which are often conducted in the presence of a high CO_2 partial pressure (e.g., for oxy-fuel combustion or the Allam cycle). $Ba_3Fe_2O_6$, on the other hand, has shown an oxygen carrying capacity of 1.25 wt%, i.e., 49.60 mol% of the Fe species in $Ba_3Fe_2O_6$ could undergo reversible redox transitions between Fe^{4+} and Fe^{3+} in each cycle, with fast redox kinetics and good cyclic stability. Given that the performance and reactivity of ternary oxides could be modified by modifying the A site and B site occupancies, there is potential to further improve formulation of $Ba_3Fe_2O_6$ as an oxygen carrier for advanced chemical looping applications such as chemical looping air separation. Therefore, in-depth studies of the oxygen uncoupling (and air separation) properties of $Ba_3Fe_2O_6$ should be carried out in the future to fully probe and exploit the potential of this ternary oxide system for chemical looping applications.

CRediT authorship contribution statement

Syed Saqline: Conceptualization, Methodology, Investigation, Writing – original draft, Writing – review & editing. **Haiming Wang:**

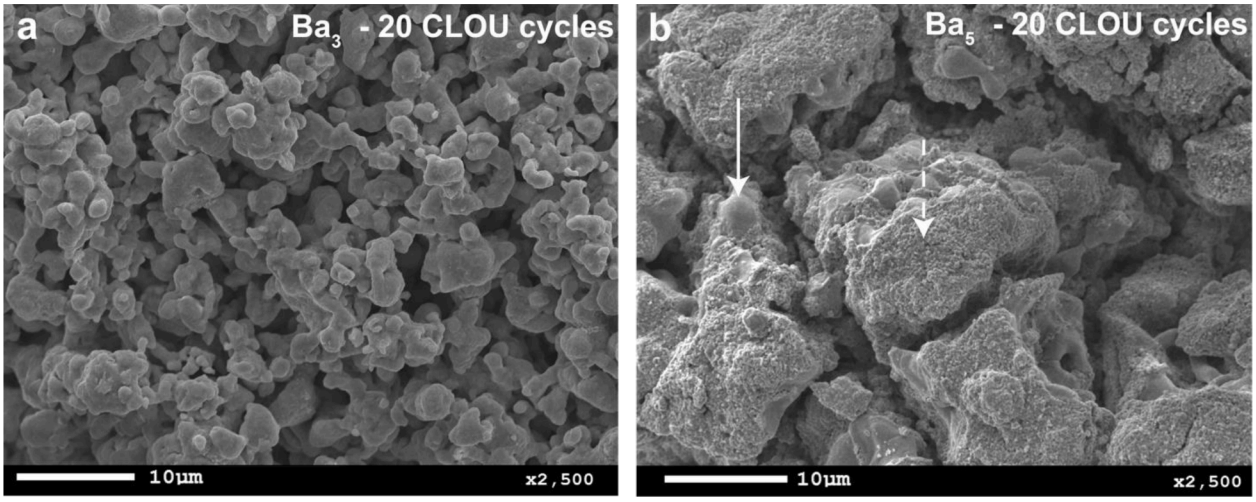

Fig. 10. SEM images of (a) and (b) - after 20 CLOU cycles.

Conceptualization, Methodology, Investigation, Writing – review & editing. **Qianwenhao Fan:** Investigation, Writing – review & editing. **Felix Donat:** Methodology, Investigation, Writing – review & editing. **Christoph Müller:** Supervision, Writing – review & editing. **Wen Liu:** Conceptualization, Supervision, Funding acquisition, Writing – review & editing.

Declaration of competing interest

The authors declare that they have no known competing financial interests or personal relationships that could have appeared to influence the work reported in this paper.

Data availability

Data will be made available on request.

Acknowledgment

The authors wish to acknowledge financial support by the National Research Foundation under its Campus for Research Excellence and Technological Enterprise (CREATE) scheme.

References

[1] Archer D. Fate of fossil fuel CO2 in geologic time. J Geophys Res Oceans 2005;110 (C9).
[2] Ritchie H, Roser M. CO2 and greenhouse gas emissions. Our world in data; 2020.
[3] IEA (2023), Tracking Clean Energy Progress 2023, IEA, Paris https://www.iea.org /reports/tracking-clean-energy-progress-2023, License: CC BY 4.0.
[4] Schnellmann MA, Görke RH, Scott SA, Dennis JS. Chemical Looping Technologies for CCS. In: Carbon Capture and Storage. The Royal Society of Chemistry; 2019. p. 189–237.
[5] Moghtaderi B. Application of chemical looping concept for air separation at high temperatures. Energy Fuels 2010;24(1):190–8.
[6] Fan LS, Li F. Chemical looping technology and its fossil energy conversion applications. Ind Eng Chem Res 2010;49(21):10200–11.
[7] Chiron FX, Patience GS. Kinetics of mixed copper–iron based oxygen carriers for hydrogen production by chemical looping water splitting. Int J Hydrog Energy 2012;37(14):10526–38.
[8] Zhu X, et al. Chemical looping beyond combustion–a perspective. Energy Environ Sci 2020;13(3):772–804.
[9] Saqline S, Chua ZY, Liu W. Coupling chemical looping combustion of solid fuels with advanced steam cycles for CO2 capture: A process modelling study. Energy Convers Manag 2021;244:114455.
[10] Saqline S, et al. Coupling chemical looping air separation with the Allam cycle–A thermodynamic analysis. J Cleaner Prod 2023;418:138097.
[11] Chang R, et al. Synthetic solid oxide sorbents for CO 2 capture: state-of-the art and future perspectives. J Mater Chem A 2022;10(4):1682–705.
[12] Dunstan MT, et al. Reversible CO2 absorption by the 6H Perovskite Ba4Sb2O9. Chem Mater 2013;25(24):4881–91.
[13] Liu W, et al. Structural evolution in synthetic, Ca-based sorbents for carbon capture. Chem Eng Sci 2016;139:15–26.
[14] González B, et al. The effect of steam on a synthetic Ca-based sorbent for carbon capture. Chem Eng J 2016;285:378–83.
[15] Liu W, et al. An investigation of the kinetics of CO2 uptake by a synthetic calcium based sorbent. Chem Eng Sci 2012;69(1):644–58.
[16] Wu X, et al. An investigation of the Ni/carbonate interfaces on dual function materials in integrated CO2 capture and utilisation cycles. Appl Catal, B 2023;338: 123053.
[17] Dou B, et al. Solid sorbents for *in-situ* CO2 removal during sorption-enhanced steam reforming process: a review. Renew Sustain Energy Rev 2016;53:536–46.
[18] Martavaltzi CS, Lemonidou AA. Hydrogen production via sorption enhanced reforming of methane: development of a novel hybrid material—reforming catalyst and CO2 sorbent. Chem Eng Sci 2010;65(14):4134–40.
[19] Lim LH, et al. A techno-economic assessment of the reutilisation of municipal solid waste incineration ash for CO2 capture from incineration flue gases by calcium looping. Chem Eng J 2023;464:142567.
[20] Bhagiyalakshmi M, Lee JY, Jang HT. Synthesis of mesoporous magnesium oxide: its application to CO2 chemisorption. Int J Greenhouse Gas Control 2010;4(1):51–6.
[21] Rodríguez N, Alonso M, Abanades J. Average activity of CaO particles in a calcium looping system. Chem Eng J 2010;156(2):388–94.
[22] MacKenzie A, et al. Economics of CO2 capture using the calcium cycle with a pressurized fluidized bed combustor. Energy Fuels 2007;21(2):920–6.
[23] Yu J, et al. CO2 capture and separations using MOFs: computational and experimental studies. Chem Rev 2017;117(14):9674–754.
[24] Kumar S, Srivastava R, Koh J. Utilization of zeolites as CO2 capturing agents: Advances and future perspectives. J CO2 Util 2020;41:101251.
[25] Gao Y, et al. Comprehensive investigation of CO 2 adsorption on Mg–Al–CO 3 LDH-derived mixed metal oxides. J Mater Chem A 2013;1(41):12782–90.
[26] Dunstan MT, et al. Large scale computational screening and experimental discovery of novel materials for high temperature CO 2 capture. Energy Environ Sci 2016;9(4):1346–60.
[27] Zhao M, et al. A novel calcium looping absorbent incorporated with polymorphic spacers for hydrogen production and CO 2 capture. Energy Environ Sci 2014;7(10): 3291–5.
[28] Zhang Y, et al. Recent advances in lithium containing ceramic based sorbents for high-temperature CO 2 capture. J Mater Chem A 2019;7(14):7962–8005.
[29] Peltzer D, et al. Characterization of potassium doped Li2ZrO3 based CO2 sorbents: Stability properties and CO2 desorption kinetics. Chem Eng J 2018;336:1–11.
[30] Ji G, et al. Experimental study on CO2 capture mechanisms using Na2ZrO3 sorbents synthesized by soft chemistry method. Chem Eng J 2017;313:646–54.
[31] Gupta K, Singh S, Rao MR. Fast, reversible CO2 capture in nanostructured Brownmillerite CaFeO2. 5. Nano Energy 2015;11:146–53.
[32] Fan LS, et al. Systems and methods of converting fuel. Google Patents; 2009.
[33] Gaultois MW, et al. Screening and characterization of ternary oxides for high-temperature carbon capture. Chem Mater 2018;30(8):2535–43.
[34] Lau CY, et al. Large scale in silico screening of materials for carbon capture through chemical looping. Energy Environ Sci 2017;10(3):818–31.
[35] Luongo G, Donat F, Müller CR. Structural and thermodynamic study of Ca A-or Co B-site substituted SrFeO 3− δ perovskites for low temperature chemical looping applications. Phys Chem Chem Phys 2020;22(17):9272–82.
[36] Marek E, et al. The use of strontium ferrite in chemical looping systems. Appl Energy 2018;223:369–82.
[37] Krzystowczyk E, et al. Substituted SrFeO 3 as robust oxygen sorbents for thermochemical air separation: correlating redox performance with compositional and structural properties. Phys Chem Chem Phys 2020;22(16):8924–32.
[38] Lyngfelt A, et al. 11,000 h of chemical-looping combustion operation—Where are we and where do we want to go? Int J Greenhouse Gas Control 2019;88:38–56.
[39] Liu G, et al. Chemical looping combustion-adsorption of HCl-containing syngas using alkaline-earth coated iron ore composites for simultaneous purification and combustion enhancement. Chem Eng J 2021;417:129226.
[40] Fan Y, Siriwardane R. Novel new oxygen carriers for chemical looping combustion of solid fuels. Energy Fuels 2014;28(3):2248–57.
[41] Siriwardane R, et al. Chemical looping coal gasification with calcium ferrite and barium ferrite via solid–solid reactions. Appl Energy 2016;165:952–66.
[42] Chen Y, et al. Investigation of perovskite supported composite oxides for chemical looping conversion of syngas. Fuel 2014;134:521–30.
[43] Fan Q, et al. Breaking the stoichiometric limit in oxygen-carrying capacity of fe-based oxygen carriers for chemical looping combustion using the Mg-Fe-O solid solution system. ACS Sustain Chem Eng 2022;10(22):7242–52.
[44] Mizusaki J, et al. Nonstoichiometry and phase relationship of the SrFeO2. 5SrFeO3 system at high temperature. J Solid State Chem 1992;99(1):166–72.
[45] Woodward P, et al. Structural studies of charge disproportionation and magnetic order in CaFeO 3. Phys Rev B 2000;62(2):844.
[46] Yamada I, et al. A perovskite containing quadrivalent iron as a charge-disproportionated ferrimagnet. Angew Chem 2008;120(37):7140–3.
[47] Zanne M, Gleitzer C, Aubry J. Barium ferrates (III-IV) for ba/fe=-phase diagrams and properties. Bull Soc Chim Fr 1971;(7):2451. -&.
[48] Abdalazeez A, et al. Syngas production from chemical looping gasification of rice husk-derived biochar over iron-based oxygen carriers modified by different alkaline earth metals. Int J Hydrog Energy 2022;47(97):40881–94.
[49] Chen J, et al. Reaction schemes of barium ferrite in biomass chemical looping gasification for hydrogen-enriched syngas generation via an outer-inner looping redox reaction mechanism. Energy Convers Manag 2019;189:81–90.
[50] Wang H, et al. Barium aluminate improved iron ore for the chemical looping combustion of syngas. Appl Energy 2020;272:115236.
[51] Montorsi M, Brisi C. NEW COMPOUND IN SYSTEM BAO-FE2O3. ANNALI DI CHIMICA 1972;62(9):641–5.
[52] Rakshit S, et al. Heat capacities of some ternary oxides in the system Ba–Fe–O using differential scanning calorimetry. J Alloys Compd 2007;438(1-2):279–84.
[53] Materials Science International Team. MSIT® info@ msiwp. com, Jozefien de Keyzer, Pierre Perrot, Myriam Sacerdote, and Andy Watson. "Barium–Iron–Oxygen: iron systems: phase diagrams, crystallographic and thermodynamic data. In: *Iron Systems, Part 1: Selected Systems from Al-B-Fe to C-Co-Fe*. Berlin, Heidelberg: Springer Berlin Heidelberg; 2008. p. 567–86.
[54] Gu H, et al. Sr2CeO4 as a robust high temperature sorbent for CO2 capture with near 100% sorbent conversion efficiency. Chem Eng J 2022;441:135942.
[55] Antao SM, Hassan I. BaCO3: high-temperature crystal structures and the Pmcn→ R3m phase transition at 811°C. Phys Chem Miner 2007;34(8):573–80.